

Propagation of Highly Efficient Star Formation in NGC 7000

Hideyuki TOUJIMA,¹ Takumi NAGAYAMA,² Toshihiro OMODAKA,^{1, 3} Toshihiro HANDA,^{4*}
Yasuhiro KOYAMA,⁵ and Hideyuki KOBAYASHI²

¹*Graduate School of Science and Engineering, Kagoshima University,
1-21-35 Korimoto, Kagoshima, Kagoshima 890-0065*

²*Mizusawa VLBI Observatory, National Astronomical Observatory of Japan,
2-21-1 Osawa, Mitaka, Tokyo 181-8588*

³*Faculty of Science, Kagoshima University,
1-21-35 Korimoto, Kagoshima, Kagoshima 890-0065*

⁴*Institute of Astronomy, The Universe of Tokyo,
2-21-1 Osawa, Mitaka, Tokyo 181-0015*

⁵*Kashima Space Research Center, National Institute of Information and Communications Technology,
893-1 Hirai, Kashima, Ibaraki 314-8510
takumi.nagayama@nao.ac.jp*

(Received 2009 October 6; accepted 2011 July 11)

Abstract

We surveyed the (1,1), (2,2), and (3,3) lines of NH₃ and the H₂O maser toward the molecular cloud L935 in the extended H II region NGC 7000 with an angular resolution of 1.6 using the Kashima 34-m telescope. We found five clumps in the NH₃ emission with a size of 0.2–1 pc and mass of 9–452 M_{\odot} . The molecular gas in these clumps has a similar gas kinetic temperature of 11–15 K and a line width of 1–2 km s⁻¹. However, they have different star formation activities such as the concentration of T-Tauri type stars and the association of H₂O maser sources. We found that these star formation activities are related to the geometry of the H II region. The clump associated with the T-Tauri type star cluster has a high star formation efficiency of 36–62%. This clump is located near the boundary of the H II region and molecular cloud. Therefore, we suggest that the star formation efficiency increases because of the triggered star formation.

Key words: Star: formation - ISM: H II region - ISM: individual (SFR) - line (NH₃)

1. Introduction

The star formation efficiencies (SFEs) of molecular clouds in the Milky Way Galaxy, are typically observed to be 10%. The SFEs in nearby molecular clouds are \simeq 3–15% (Swift & Welch 2008; Evans et al. 2009). The observations of giant molecular clouds in the inner Galaxy indicate that the SFEs in these clouds are of the order of a few percent (Myers et al. 1986). However, Lada (1992) found that three of five massive cores, NGC 2024, NGC 2068, and NGC 2071 exhibit higher SFEs of \simeq 30–40%. It remains unclear why these SFEs are high. Lada (1992) suggested that the high gas densities and high gas mass may be required for the high SFE but there should be additional conditions, because the other two cores exhibit low SFEs of \simeq 7%. However, additional conditions for high SFE are unknown, and more observational investigations are required. *

NGC 7000 is an extended H II region in the Cygnus X region. On its southeastern side is a molecular cloud L935. The ¹³CO emission in this molecular cloud is the brightest in the Cygnus X region (Dobashi et al. 1994).

Figure 1 shows the optical image of NGC 7000 and L935. Seven T-Tauri stars are clearly clustered at the boundary of the H II region (Herbig 1958). This suggests that the star formation is triggered by the interaction of the H II region with the dense molecular gas. A number of studies of star formation in a cloud associated with an H II region have been performed (Sugitani et al. 1989; Sugitani et al. 1991; Sugitani & Ogura 1994; Dobashi et al. 2001; Deharveng et al. 2003; Deharveng et al. 2005). For example, in the nearby H II region, IC 5070, a molecular shell with an expanding velocity of 5 km s⁻¹, is found in the ¹²CO ($J=1-0$) line (Bally & Scoville 1980). They suggest that the T-Tauri type stars in IC 5070 are formed by the expanding shell.

Our aim is to investigate the relationship between dense molecular gas and star formation based on the SFE. NGC700 has the advantage of allowing us to estimate the SFE because T-Tauri type stars are associated with it and we can estimate the stellar mass accurately. Therefore, we made the observations in the NH₃ line to estimate the mass of dense molecular gas. We also surveyed an H₂O maser source that is associated with outflow from a young stellar object (YSO). We adopted the distance to NGC 7000 to be 600 pc (Laugalys & Straižys 2002).

* Present address: Graduate School of Science and Engineering, Kagoshima University, 1-21-35 Korimoto, Kagoshima, Kagoshima 890-0065.

2. Observations

2.1. NH_3 Observations

We observed NGC 7000 in the NH_3 lines with the Kashima 34-m telescope of the National Institute of Information and Communications Technology (NiCT) from April 2007 to October 2008. We made simultaneous observations in three inversion transitions of the NH_3 (J, K) = (1,1), (2,2), and (3,3) lines at 23.694495, 23.722633, and 23.870129 GHz, respectively. At 23 GHz, the telescope beam size was $1''.6$ and the main beam efficiency (η_{MB}) was 0.50. We used a K -band HEMT amplifier whose system noise temperature was 150–250 K. The relative pointing error was better than $0''.2$; this was checked by the observations of several H_2O maser sources at 22.235080 GHz. All spectra were obtained with an 8192-channel FX-type spectrometer developed at Kagoshima University and NiCT. Its bandwidth and frequency resolution are 256 MHz and 31.25 kHz, respectively. The corresponding velocity coverage and velocity resolutions are 3200 km s^{-1} and 0.39 km s^{-1} at the NH_3 frequencies, respectively. The total number of the observed positions is 311 and the surveyed area is approximately $38' \times 11'$ or $6.6 \text{ pc} \times 1.9 \text{ pc}$. The NH_3 profiles were obtained at $1'$ grid points of the equatorial coordinates. All data were obtained with the position switch between the target and a reference position. The reference position is $(\alpha, \delta)_{(\text{J2000})} = (20^{\text{h}}58^{\text{m}}02^{\text{s}}.1, +44^{\circ}04'24'')$, where no NH_3 emission was detected. We integrated at least 20 min at each point. The rms noise level was typically 0.20 K in the unit of the main beam brightness temperature defined by $T_{\text{MB}} \equiv T_{\text{A}}^*/\eta_{\text{MB}}$, where T_{A}^* is the antenna temperature calibrated by the chopper wheel method (Kutner & Ulich 1981).

Data reduction was performed using the UltraSTAR package developed by the radio astronomy group at the University of Tokyo (Nakajima et al. 2007). In this paper, the intensities are presented in the main beam temperature.

2.2. H_2O Maser Observations

The single-dish observations of the $6_{16} \rightarrow 5_{23}$ transition of the H_2O maser at 22.235080 GHz were made at the positions of the NH_3 emission peaks. The observations were made with the Kashima 34-m telescope and the VLBI Exploration of Radio Astrometry (VERA) Iriki 20-m telescope. In the observations made with the Kashima 34-m telescope, the conversion factor from the antenna temperature to the flux density was 8 Jy K^{-1} for a point source. The rms noise level of the H_2O maser spectra was less than 1 Jy after integration of 10–30 min. The velocity resolution of the spectrometer was 0.42 km s^{-1} at the H_2O maser frequency. In the observations made with the VERA Iriki 20-m telescope, the conversion factor from the antenna temperature to the flux density was 20 Jy K^{-1} . The rms noise level of the H_2O maser spectra was less than 1 Jy after integration of 30 min. The velocity resolution of the spectrometer was 0.21 km s^{-1} at the H_2O maser frequency.

The VLBI observations of the $6_{16} \rightarrow 5_{23}$ transition of the H_2O maser were made with the VERA of the National Astronomical Observatory of Japan (NAOJ) on February 15, 2008. The data were recorded using the VSOP terminal at a rate of 128 Mbit s^{-1} . The recorded signals were correlated using the Mitaka FX correlator. The spectral resolution was set at 31.25 kHz, which corresponds to a velocity resolution of 0.42 km s^{-1} . The system noise temperature is approximately 140 K. The phase calibrator was BL Lac (ICRF J220243.2+421639). The phase-tracking center of the array was set at $\alpha(\text{J2000}) = 20^{\text{h}}57^{\text{m}}56^{\text{s}}.717$, $\delta(\text{J2000}) = +43^{\circ}53'39''.60$. We calibrated the data in the standard reduction procedure with the Astronomical Image Processing System (AIPS) of the National Radio Astronomy Observatory (NRAO). The resultant rms noise level and synthesized beam size are $\simeq 1 \text{ Jy beam}^{-1}$ and $\simeq 1.4 \times 0.7 \text{ mas}$ with a position angle of -46° .

3. Results

3.1. Distribution of NH_3 Clumps

We observed 311 positions in the survey. NH_3 (1,1) and (2,2) lines were detected with a signal-to-noise ratio greater than 3 at 138 and 32 positions, respectively. The (3,3) line was not detected at any positions in the observed area. We show the profiles towards emission peaks in Figure 2.

Figure 3 shows the velocity integrated map of the main hyperfine component of the NH_3 (1,1) line over $v_{\text{LSR}} = -3$ to 8 km s^{-1} . The NH_3 (1,1) emission extends over $38' \times 11'$ or $6.6 \text{ pc} \times 1.9 \text{ pc}$. The distribution is elongated in the northeast-southwest direction.

We define a *clump* as an isolated feature in the (1,1) integrated intensity distribution with intensities stronger than the 3σ noise level ($\gtrsim 0.6 \text{ K km s}^{-1}$) both in the (1,1) and the (2,2) lines. Based on this definition, we identify two NH_3 clumps; we call them clump-A at the northeast and clump-B at the southwest. We found local peaks in these clumps. In clump-A, there are YSOs that may have been formed near three local peaks (see subsection 4.1). In order to investigate the star formation of clump-A in detail, we define three *subclumps* as three local peaks in clump-A. We call them subclump-A1, subclump-A2, and subclump-A3 from the east to the west. The parameters of the clumps and subclumps are summarized in Table 1. As shown in Figure 3, the shape of these subclumps appears to be an ellipse with the major axis along the right ascension and the minor axis along the declination. Therefore, we estimate the subclump sizes of the major and minor axes using the FWHM of the Gaussian fitting to the intensities along the right ascension and declination, respectively. Figure 4 shows the results of the Gaussian fitting. This size is used to estimate the mass of each subclump.

Clump-A extends over $11' \times 10'$ or $1.9 \text{ pc} \times 1.8 \text{ pc}$ (Figure 3). The velocity channel maps from $v_{\text{LSR}} = 0$ to 8 km s^{-1} are shown in Figure 5. Clump-A appears at $v_{\text{LSR}} = 5\text{--}7 \text{ km s}^{-1}$ and clump-B appears at $v_{\text{LSR}} = 1\text{--}3 \text{ km s}^{-1}$.

Figure 6 shows the position-velocity diagram along the dashed line shown in Figure 3. Clump-A and clump-B are clearly separated in the position-velocity space. It suggests that these clumps are not parts of a single object. However, clump-A, clump-B, and other weak features between the clumps are aligned on the position-velocity diagram. This suggests that these clumps may be formed from a single system (see subsection 4.3).

A velocity gradient is found in subclump-A3. Figure 7 shows the position-velocity diagram of subclump-A3. The estimated velocity gradient is $1.66 \pm 0.57 \text{ km s}^{-1} \text{ pc}^{-1}$. The linewidth of the peak spectrum is $2.11 \pm 0.08 \text{ km s}^{-1}$, and it is 1.4 times broader than the other spectra in clump-A. The other subclumps do not show the velocity gradient.

Clump-B extends over $15' \times 19'$ or $2.6 \text{ pc} \times 3.3 \text{ pc}$ (Figure 3). In the velocity channel maps, clump-B appears at $v_{\text{LSR}} = 1\text{--}4 \text{ km s}^{-1}$ (Figure 5). A velocity gradient is found in the emission peak of clump-B. Figure 7 shows the position-velocity diagram of the peak of clump-B. The estimated velocity gradient is $-1.26 \pm 0.23 \text{ km s}^{-1} \text{ pc}^{-1}$.

The ¹³CO ($J=1\text{--}0$) emission was detected by Dobashi et al. (1994) with a velocity range of $v_{\text{LSR}} = 1.5\text{--}7.5 \text{ km s}^{-1}$ at the mid position of clump-A and clump-B. It comprises two velocity components of clump-A and clump-B. The spatial distribution in the NH₃ line is similar to that in ¹³CO line, although the ¹³CO observations were made with a lower angular resolution ($2.7'$) and sparsed sampling ($5'$). Clump-B is located at the CO peak both on the sky and in the velocity. Clump-A is located on the northeast side of the CO cloud; it faces the H II region.

3.2. Physical Parameters of Clumps and Subclumps

We estimated the physical parameters of the clumps and the subclumps. NH₃ is a very well-studied molecule with which to investigate the physical conditions of the dense molecular gas.

The NH₃ lines are split by the quadrupole hyperfine interaction. Optical depths can be directly determined from the intensity ratio of the main to the satellite lines. Because we detect the hyperfine structure in the (1,1) line, the optical depth, $\tau_{(1,1)}$, can be derived from the intensity ratio. Figure 8 shows the correlation of the integrated intensities of the main and the satellite lines. We estimated two intensity ratios of the inner and outer satellite lines to the main line. The optical depths estimated from these two ratios are the same within the error. We list the optical depths of the clumps and the subclumps in Table 2, and these are found to be in the range of 0.8–1.6.

We estimated the NH₃ rotational temperature from the intensity ratio of the (2,2) line to the (1,1) line using the method shown by Ho & Townes (1983). Figure 9 shows the correlations of the integrated intensities in the (1,1) and (2,2) lines. The rotational temperatures of all clumps and subclumps are 11–15 K and the same within the error. Using the collisional excitation model (Walmsley & Ungerechts 1983; Danby et al. 1988), the rotational temperature is estimated to be very close to the gas kinetic temperature, T_{kin} , for $T_{\text{rot}} < 15 \text{ K}$. Therefore, T_{kin} should

be approximately 13 K. The estimated temperatures are listed in Table 2.

We derive the total column density of NH₃, $N(\text{NH}_3)$, from the column density in the (1,1) line, assuming the local thermodynamic equilibrium (LTE) condition for the molecules in the clumps (Rohlfs & Wilson 1996). The estimated total column densities of the clumps are listed in Table 2 and they are in the range of $N(\text{NH}_3) = (1.8\text{--}3.7) \times 10^{15} \text{ cm}^{-2}$.

We derived the molecular gas mass for each of the clumps and subclumps using two methods. One is the LTE mass that is derived from the deconvolved size and the column density with the assumed abundance ratio. Using a model of a uniform density share with 40% helium in mass, the LTE mass is given by

$$M_{\text{LTE}} = 467 \left(\frac{R}{[\text{pc}]} \right)^2 \left(\frac{N(\text{NH}_3)}{10^{15} [\text{cm}^{-2}]} \right) \left(\frac{X(\text{NH}_3)}{10^{-7}} \right)^{-1} M_{\oplus}$$

where R is the radius of the sphere, and $X(\text{NH}_3)$ is the abundance of NH₃ relative to H₂. For clump-A and B, R is given from a geometrical mean of the major and minor axes of an apparent ellipse after beam deconvolution. For subclumps A1–A3, R is given from a geometrical mean of FWHMs of the Gaussian fitting along the right ascension and declination. The estimated sizes in diameter are in the range of 0.6–1 pc for the clumps and 0.2–0.3 pc for the subclumps.

Ho & Townes (1983) reviewed that the abundance of NH₃ relative to H₂ has been estimated to range from 10^{-7} in the core of the dark cloud L183 (Ungerechts et al. 1980) up to 10^{-5} in the hot core of the Orion KL (Genzel et al. 1982) and the ion-molecule chemistry produces an abundance of the order of 10^{-8} (Prasad & Huntress 1980). We use the abundance ratio of 10^{-7} , because the estimated kinetic temperature and the clump size in NGC 7000 are close to those of L183. Using this abundance, the hydrogen column density derived from NH₃ is derived to be $N(\text{H}_2) = (1.8\text{--}3.7) \times 10^{22} \text{ cm}^{-2}$. This corresponds to $A_V \simeq 10\text{--}20 \text{ mag}$ by assuming the conversion factor from the relation $N(\text{H}_2)/A_V = 1.87 \times 10^{21} \text{ atoms cm}^{-2} \text{ mag}^{-1}$ (Bohlin et al. 1978). Comerón & Pasquali (2005) estimated the extinction of the molecular cloud to be $A_V \simeq 10\text{--}30 \text{ mag}$ using 2 MASS archive data. These two values of A_V are consistent within a factor. Moreover, the hydrogen column density estimated from ¹³CO (Dobashi et al. 1994) is consistent with our estimation within a factor of 2–3, although the observation grid is different. The LTE masses of clump-A and clump-B are estimated to be 95 and 452 M_{\odot} , respectively. The LTE masses of subclump-A1, subclump-A2, and subclump-A3 are estimated to be 12, 20, and 9 M_{\odot} , respectively.

The other mass estimation is the virial mass, M_{vir} . This is calculated as $M_{\text{vir}} = kR\Delta v^2 M_{\odot}$, where k is taken as 210 based on a uniform density sphere (MacLaren et al. 1988), R is the radius of the clump, and Δv is the half-power line width. The virial masses of clump-A and clump-B are estimated to be 125 and 350 M_{\odot} , respectively. The virial masses of subclump-A1, subclump-A2, and subclump-A3 are not estimated, because their sizes are small.

We found that the LTE mass and the virial mass are consistent by a factor of 1.3. From the above mentioned comparisons such as A_V , ^{13}CO , and derived mass, we could estimate the actual masses of molecular gas within a factor of 2–3. All these derived parameters are summarized in Table 2.

3.3. H_2O Maser Source in Subclump-A2

We conducted an H_2O maser survey of the NH_3 clumps and subclumps. We discovered a new H_2O maser emission at the NH_3 peak in subclump-A2. However, no H_2O maser emission was detected in the others with the upper limit of 3 Jy (Figure 3).

We conducted monitoring observations of the maser source from August 2007 to May 2008. The obtained spectra are shown in Figure 10. All spectra show a single velocity component with a narrow linewidth (FWHM) of $\simeq 1 \text{ km s}^{-1}$. This maser emission is time-variable between 107 Jy in December 2007 and 5 Jy in May 2008. We found that the maser emission disappeared with the upper limit of 2.1 Jy in October 2008. The LSR velocity of the maser jumped from 8.4 to 9.0 km s^{-1} during the period from November 2007 to December 2007, and from 9.0 to 9.6 km s^{-1} from January 2008 to April 2008. This means that there were two maser spots and the lifetime of each spot is less than a year.

Claussen et al. (1996) reported that an H_2O maser associated with a low-mass star is variable on a timescale ranging from months to a year. The H_2O maser in subclump-A2 shows variations on the same timescale. Therefore, the H_2O maser should be associated with low-mass stars.

The detected H_2O maser of $v_{\text{LSR}} \simeq 9 \text{ km s}^{-1}$ is red-shifted with respect to the ambient gas velocity of $\simeq 5 \text{ km s}^{-1}$ observed in the NH_3 line. This suggests that the maser may be associated with outflows from the protostar.

To identify the counterpart of the maser, we should obtain an accurate position of the maser. Therefore, we conducted VLBI observations on February 15, 2008, to determine its position. A single feature with a size of $1.6 \text{ mas} \times 0.7 \text{ mas}$ or $0.96 \times 0.42 \text{ AU}$ was detected. The position of this maser feature was obtained to be $(\alpha, \delta)_{\text{J2000}} = (20^{\text{h}}57^{\text{m}}57^{\text{s}}01, +43^{\circ}53'28''.5)$ by a fringe rate analysis. The position uncertainty was approximately $0''.1$. However, we can find no visible star or optical feature suggesting an outflow at the position of the maser in the DSS2 images. We discuss the counterpart of the maser in subsection 4.1.

4. Discussion

4.1. Observed Star Formation Activity in Each Clump and Subclump

To investigate the star formation in our identified NH_3 clumps, we examined the distribution of young stars reported in the previous observations. In clump-A, Herbig (1958) found seven emission-line stars, and Cohen & Kuhl (1979) confirmed that these stars are T-Tauri type stars. T-Tauri type stars are suitable for the mass estimation because their mass can be well estimated using the H-R

diagram (Cohen & Kuhl 1979). We estimate the mean and total masses of T-Tauri type stars in clump-A to be 1.3 and 9.0 M_{\odot} , respectively. We consider that these T-Tauri type stars indicate the lower limit of the star formation activity. We found 32 and 11 infrared sources listed in the 2MASS and MSX catalogues, respectively, in clump-A. We consider that these infrared sources indicate the upper limit of the star formation activity, although some of these sources may be the fore/background sources. There is a large difference in the distribution of these T-Tauri type stars and infrared sources in each subclump, suggesting differences in star formation activity.

We found that five of seven T-Tauri type stars are concentrated in subclump-A1. The total mass of these T-Tauri stars is 6.9 M_{\odot} . The concentration of the T-Tauri type stars suggests that the star formation of subclump-A1 is the most active. There are 15 2MASS sources and 3 MSX sources in subclump-A1. The T-Tauri type stars and the majority of 2MASS sources are found on the east side of subclump-A1, where the HII region is located.

We found a new H_2O maser source in subclump-A2. Furuya et al. (2003) reported that $\simeq 40\%$ of class 0, $\simeq 4\%$ of class I, and no class II low-mass protostars emit the H_2O maser. We found the counterpart of the H_2O maser in the *Spitzer* infrared images at 24 and 70 μm (Figure 11). The 70 μm emission of the counterpart is centered at $(\alpha, \delta)_{\text{J2000}} = (20^{\text{h}}57^{\text{m}}57^{\text{s}}33, +43^{\circ}53'27''.9)$ and extends over a $20 \times 20''$ ($12000 \times 12000 \text{ AU}$) area. The position of the counterpart is consistent with that of the H_2O maser obtained by our VLBI observations. The *Spitzer* source should be a protostar associated with the H_2O maser. We show a spectrum of the *Spitzer* source at six wavelengths in Figure 12. At the wavelengths of 1.25–8.28 μm , the counterpart is not detected with 2MASS and MSX, and we show the upper limits. A single-temperature black-body radiation through the data points at 24 and 70 μm is consistent with the upper limits. Its bolometric luminosity is estimated to be 42 L_{\odot} . Both the spectrum shape and the bolometric luminosity are consistent with those of a class 0 protostar (Bachiller 1996). Therefore, the counterpart of the H_2O maser should be a class 0 protostar. To confirm this, the submillimeter observations are required.

One T-Tauri type star and 5 2MASS sources are found in subclump-A2. A nebulosity at $(\alpha, \delta)_{\text{J2000}} = (20^{\text{h}}57^{\text{m}}55^{\text{s}}, +43^{\circ}53'40'')$ is visible in the DSS2 images in the *B*, *R*, and *I*-bands. This is considered to be a reflection nebula, because it is continuously detected at the optical wavelength.

T-Tauri type stars are not found in subclump-A3. Four 2MASS and four MSX sources are found. These MSX sources would be the YSOs embedded in the dust envelope because they are invisible in the DSS2 and 2MASS images. G085.0482-01.1330 identified by MSX is located at the peak position of the (1,1) line in subclump-A3. We found a velocity gradient at this position (see subsection 3.1). The velocity gradient would be due to the simple core rotation or the outflow from G085.0482-01.1330. This source is located at the center of the velocity gradient. The spectrum of this source, shown in Figure 12,

is similar to that of a class I protostar. The bolometric luminosity was estimated to be $190 L_{\odot}$.

T-Tauri type stars and H₂O maser sources are not found in clump-B. We found 24 2MASS and 6 MSX sources. One of the MSX sources identified as G084.8235-01.1094, is located at the peak position in the (1,1) line. The velocity gradient is found in the (1,1) line at this position. The spectrum of this source, shown in Figure 12, is similar to that of a class I protostar. Its bolometric luminosity was estimated to be $230 L_{\odot}$.

We consider that the star formation of clump-A is more active than that of clump-B. In clump-A, both the number and the total mass of stars in subclump-A1 are larger than those of subclump-A2 and A3.

4.2. Star Formation Efficiency

We have presented the stellar mass of each clump in the previous subsection. In this subsection, we examine the relation between the stellar and the molecular gas masses. We estimate the star formation efficiency given by $SFE = M_{\text{star}} / (M_{\text{star}} + M_{\text{gas}})$.

The SFE of subclump-A1 is estimated to be $\simeq 36\%$ from the stellar mass of $6.9 M_{\odot}$ and gas mass of $12 M_{\odot}$. We use the stellar mass of the identified T-Tauri type stars in this estimation. However, other T-Tauri type stars may be associated with the NH₃ clumps but located just behind them. In this case, these T-Tauri type stars could be detected in the *K*-band of 2MASS. We obtained the extinction in the *K*-band to be $A_K \simeq 1$ mag using $A_V \simeq 10$ mag estimated from the NH₃ column density and the extinction law of $A_K/A_V = 0.112$ (Rieke & Lebofsky 1985). For the identified T-Tauri type stars, the *K*-band magnitude of 2MASS is 8.5–11.5 mag. Therefore, the *K*-band magnitude of a T-Tauri type star located behind the clumps is estimated to be 9.5–12.5 mag. This value is brighter than the 2MASS *K*-band detection limit of 14.3 mag (SNR = 10). We found ten 2MASS sources that are not identified as T-Tauri type stars in subclump-A1. In the case that all of them are T-Tauri type stars with a mass of $1.3 M_{\odot}$, the SFE of subclump-A1 increases to $\simeq 69\%$.

In subclump-A2, a T-Tauri type star with a mass of $0.8 M_{\odot}$ is found. Therefore, its SFE is estimated to be $\simeq 4\%$ from the gas mass of $20 M_{\odot}$. The SFE averaged over the whole clump-A is estimated to be $\simeq 8\%$ from the stellar mass of $7.7 M_{\odot}$ and gas mass of $95 M_{\odot}$. The SFEs of both subclump-A3 and clump-B might be 0% because no T-Tauri type star is found there. In the case that the 2MASS sources are included in the stellar mass estimation, the SFEs of subclump-A2, A3, and the whole of clump-A are estimated to be 23–36%. This value is close to the SFE of subclump-A1. However, clump-B shows lower SFE of 6% even in this case.

In either case, including only T-Tauri type stars or also the 2MASS sources, the SFE of subclump-A1 is estimated to be 36–62%; this is higher than the SFEs of the other molecular clouds. In order to make a fair comparison, we revisited the SFEs of the following three molecular clouds using the same procedure. The SFE of NGC 2264 is estimated to be 11% from the stellar mass of the OB

and T-Tauri type stars of $119 M_{\odot}$ (Dahm & Simon 2005) and the molecular gas mass traced in the NH₃ line of $1000 M_{\odot}$ (Lang & Willson 1980). The SFE of NGC 1333 is estimated to be 16% from the stellar mass of the T-Tauri type stars of $17 M_{\odot}$ (Aspin 2003) and the molecular gas mass traced in the NH₃ line of $106 M_{\odot}$ (Ladd et al. 1994). The SFE of L1228 is estimated to be 8% from the stellar mass of the T-Tauri type stars of $1 M_{\odot}$ (Kun et al. 2009) and the molecular gas mass traced in the NH₃ line of $12 M_{\odot}$ (Anglada et al. 1994). The SFE of subclump-A1 is close to $\simeq 42\%$ estimated at NGC 2024 and NGC 2068 from the CS observations (Lada 1992). The derived SFEs of individual clumps are summarized in Table 3. The values of “Total” in Table 3 correspond to the upper limits of the SFEs for the case in which the all 2MASS sources we found are associated with the clump or the subclump.

4.3. Geometry

Although clump-A and clump-B are adjacent on the sky, there is a big difference in the star formation activities. Because these clumps are close to NGC 7000, the difference may be due to the H II region. Therefore, we discuss the geometry of the clumps and the H II region.

The optical image (Figure 1) shows that the clumps are located in the foreground of the H II region. Subclump-A1 is the nearest to and clump-B is the farthest from the H II region on the sky.

To investigate the three-dimensional structure of clump-A, we estimated the length along the line of sight, l , derived as $l = N(\text{H}_2)/n_{\text{cr}}$, where $N(\text{H}_2)$ and n_{cr} are the hydrogen column density and the critical density in the NH₃ line, respectively. When we use $n_{\text{cr}} \simeq 10^4 \text{ cm}^{-3}$ (Myers & Benson 1983), the lengths of subclump-A1, A2, and A3 are estimated to be $l \simeq 0.8, 0.6, \text{ and } 0.6 \text{ pc}$, respectively. These values are 2–3 times longer than the sizes on the sky. The three subclumps may be the end-on view of the elephant trunks observed in M16.

As seen in subsection 3.2, clump-A and clump-B are spatially separated. This suggests that these two clumps are gravitationally unbound. The total LTE mass of the two clumps is $547 M_{\odot}$. If the two clumps are gravitationally bound, the enclosed mass is estimated to be $11000 M_{\odot}$ from their separation of 2.9 pc and relative velocity of 4 km s^{-1} . The LTE mass is $\sim 1/20$ of the enclosed mass. The mass of the cloud around the two clumps traced in the ¹³CO line is estimated to be $3400 M_{\odot}$ from the column density of $1.15 \times 10^{22} \text{ cm}^{-2}$ (Dobashi et al. 1994). Both the total mass of the two clumps and the ¹³CO cloud is smaller than the enclosed mass. Therefore, clump-A and clump-B are gravitationally unbound. However, clump-A, clump-B, and other weak features between the clumps are aligned on the position-velocity diagram (Figure 6). This suggests that they are also aligned in the three-dimensional structure.

We compare the LSR velocities of the H II region and the molecular gas. Figure 13(a) shows the LSR velocity map of the H α emission (Fountain et al. 1983) superimposed on the ¹³CO integrated intensity map (Dobashi et al. 1994)

and the NH_3 (1,1) integrated intensity map. The LSR velocity of the $\text{H}\alpha$ emission line is approximately 0 km s^{-1} at the position overlapped with the NH_3 clumps, and $4\text{--}5 \text{ km s}^{-1}$ on both the eastern and the western sides of the NH_3 clumps. The LSR velocities of clump-A and clump-B are 5.5 and 1.5 km s^{-1} , respectively. Clump-A is redshifted with respect to the H II region. We show the FWHM map of the $\text{H}\alpha$ emission (Fountain et al. 1983) in Figure 13(b). The FWHM of the $\text{H}\alpha$ emission around the NH_3 clumps is $10\text{--}20 \text{ km s}^{-1}$. This value is narrower than the FWHM at the other position. These characteristics can be interpreted as indicating that the redshifted component of the $\text{H}\alpha$ emission is blocked by clump-A, and only ionized gas located in the foreground of clump-A would be observed. Therefore, clump-A would be surrounded by the ionized gas.

In clump-B, the $\text{H}\alpha$ emission is not detected. This indicates that there is no ionized gas at the foreground of clump-B. However, we found the presence of ionized gas in the background of clump-B, because a radio continuum emission at 4.8 GHz is detected there (Wendker 1984). Therefore, clump-B would be located in the foreground of the H II region. We show the schematic geometry of the NH_3 clumps and the H II region in Figure 14.

4.4. Why is the SFE of Subclump-A1 high?

In subsection 4.2, we show that the SFE $\simeq 36\text{--}62\%$ of subclump-A1 is higher than that of other molecular clouds. Here, we examine why this is so.

There is no difference in the physical condition of the molecular gas in clump-A and clump-B. The kinetic temperature and the velocity width of clump-A are similar to those of clump-B. The main difference between them appears to be the geometry to the H II region. The geometry shown in the previous subsection suggests that subclump-A1 is closer to the H II region than any of the other subclumps or clump-B. The five T-Tauri stars in subclump-A1 would be formed by the interaction of the H II region with the molecular gas. A high SFE is observed in other triggered star forming regions. The NGC 2024 and 2068 molecular clouds, each of which interact with an H II region (Chandler & Carlstrom 1996), show SFE $\simeq 42\%$ (Lada 1992). This means that the SFE of subclump-A1 increases because of the effect of the H II region.

Theoretical calculations suggest that the SFE is in the range of $30\text{--}50\%$ of the regions that form clusters of low-mass stars (Matzner & McKee 2000). The estimated SFE of subclump-A1 is very close to this value. Matzner & McKee (2000) suggest that the SFE of the clumps that are more massive than approximately $3000 M_\odot$, in which O stars will form, is lower than $30\text{--}50\%$ because of the destructive effects of massive stars. The SFE may be increased in a cloud with the formation of a low-mass star cluster.

We consider whether other subclumps and clump-B are kept the low SFE. Star formation appears to advance sequentially in the order of A1, A2, A3, and B. This order is the same as that of the distance from the H II region. It

is suggested that the triggered star formation or the interstellar shock comes sequentially from the H II region. A molecular shell with an expansion velocity of $\simeq 5 \text{ km s}^{-1}$ is found in the ^{12}CO line (Bally & Scoville 1980). In the case that the effect of the H II region expands at this velocity, the crossing timescale from subclump-A1 to clump-B is estimated to be $\simeq 6 \times 10^5 \text{ yr}$ using their separation of 2.9 pc . This timescale is shorter than the lifetime of the O5 V type star ($2 \times 10^6 \text{ yr}$; Walborn 2007), which is considered to be the ionizing star of the H II region (Comerón & Pasquali 2005). This suggests that the H II region can affect clump-B in the future, in the case that the separation in the line of sight is the same order of magnitude as that on the sky. The total molecular gas mass of clump-A and clump-B is $391 M_\odot$. This mass is close to that of NGC 2024 or NGC 2068 (Lada 1992), and it is small enough to avoid cloud destruction by new born stars (Matzner & McKee 2000). This suggests that the SFE of the combined clump-A and B can be as high as approximately 40% .

The observed SFE is sensitive to the estimation of both gas and stellar masses. As mentioned in subsection 3.2, we estimated the actual gas mass within a factor of $2\text{--}3$. However, it is generally difficult to estimate the molecular gas mass. The estimated molecular gas mass is sometimes different by more than a factor of 10 in different observed lines. In the W3 giant molecular cloud, the molecular gas mass estimated in the ^{12}CO ($J=1\text{--}0$), C^{18}O ($J=2\text{--}1$), and NH_3 lines is 16000 , 1400 , and $3300 M_\odot$, respectively (Tieftrunk et al. 1998), although they were estimated in the same area. For the estimation of SFE, the ^{12}CO line data are often used to estimate the molecular gas mass (e.g. Myers et al. 1986; Leisawitz et al. 1989). Because the ^{12}CO line traces the less dense gas, the molecular gas mass might be overestimated. However, the data of the molecular line to trace the dense gas is not ideal to estimate the molecular gas mass, because the relative abundance is difficult to determine precisely. For example, the abundance of NH_3 varies by up to a factor of 10 from cloud to cloud.

It is also difficult to estimate the stellar mass accurately. There are few studies based on total stellar mass estimated as the sum of the masses of individual stars. Although the infrared luminosity is often used to estimate the stellar mass, it would be less accurate than the mass estimated based on the number count of the T-Tauri type stars shown in this paper.

As mentioned above, the observed SFE reported in some studies should be revised by an order of magnitude. The SFEs of the nearby molecular clouds such as Perseus and Ophiuchus, L1551 in Taurus, and giant molecular clouds in the inner Galaxy are $3\text{--}6\%$, $9\text{--}15\%$, and 2% , respectively (Myers et al. 1986; Swift & Welch 2008; Evans et al. 2009). These values may be underestimated, because these studies use the molecular gas mass estimated from the A_V and CO maps. We should take care how to estimate the SFE to refer it from the previous studies.

4.5. Future H₂O Maser Surveys

Previous surveys of H₂O masers have been carried out based on the IRAS Point Source Catalogue (PSC). This catalogue is useful for searching for YSOs embedded in the molecular clouds. However, the counterpart of the H₂O maser that we found in subclump-A2 is not catalogued. It shows that the H₂O survey based on the IRAS PSC is insufficient. There are two possibilities why some YSOs are uncatalogued in the IRAS PSC: sensitivity too poor to detect them or resolution too poor to resolve a cluster of some sources. Figure 15 shows an IRAS image at 100 μ m overlayed on our NH₃ map. A complex source is found near clump-A in the IRAS image, although it is composed of several infrared sources in the *Spitzer* image (see Figure 11).

This suggests that there are many H₂O maser sources which are not catalogued in the IRAS PSC. A new H₂O maser survey should be carried out based on a point source catalogue with a higher resolution and sensitivity, such as *Spitzer* and/or AKARI should be carried out. Our new H₂O maser is associated with a far-infrared source, and its luminosity is brighter than that of the mid-infrared. This characteristic may be a good criterion with which to find new H₂O maser sources.

5. Conclusions

We observed NGC 7000 in the NH₃ line and H₂O maser using the Kashima 34-m telescope. Our observations are summarized as follows:

1. We found two major clumps with a mass of 95–452 M_{\odot} , and three subclumps with a mass of 9–20 M_{\odot} . The molecular gas in these show similar gas kinetic temperatures of 11–15 K and line width of 1–2 km s⁻¹. However, they show different star formation activities such as the concentration of T-Tauri type stars and the association of an H₂O maser.
2. One of the clumps that is associated with a cluster of T-Tauri type stars shows the SFE \simeq 36–62%. This SFE is higher than that of the other clumps.
3. A comparison of the distribution of molecular gas and ionized gas traced by the H α emission suggests that the clump with high SFE is located near the H II region. Therefore, the high SFE would be related to the interaction of molecular gas and the H II region.
4. We found a new H₂O maser source in the NH₃ clump. Although the counterpart of this maser is not found in the IRAS point source catalogue, we found it in the *Spitzer* 24- and 70- μ m images. This suggests that a new H₂O maser survey should be carried out based on the point source catalogue of *Spitzer* and/or AKARI.

We thank an anonymous referee for very useful comments and suggestions. T.O. was supported by a Grant-in-Aid for Scientific Research from the Japan Society for the Promotion Science (17340055). We acknowledge K.

Miyazawa (NAOJ) for his technical support of observations.

References

- Anglada, G., Rodriguez, L. F., Girart, J. M., Estalella, R., & Torrelles, J. M. 1994, *ApJL*, 420, L91
- Aspin, C. 2003, *AJ*, 125, 1480
- Bachiller, R. 1996, *ARA&A*, 34, 111
- Bally, J., & Scoville, N. Z. 1980, *ApJ*, 239, 121
- Bohlin, R. C., Savage, B. D., & Drake, J. F. 1978, *ApJ*, 224, 132
- Cambr  sy, L., Beichman, C. A., Jarrett, T. H., & Cutri, R. M. 2002, *AJ*, 123, 2559
- Chandler, C. J., & Carlstrom, J. E. 1996, *ApJ*, 466, 338
- Claussen, M. J., Wilking, B. A., Benson, P. J., Wootten, A., Myers, P. C., & Terebey, S. 1996, *ApJS*, 106, 111
- Codella, C., Welser, R., Henkel, C., Benson, P. J., & Myers, P. C. 1997, *A&A*, 324, 203
- Cohen, M., & Kuhl, L. V. 1979, *ApJS*, 41, 743
- Comer  n, F., & Pasquali, A. 2005, *A&A*, 430, 541
- Dahm, S. E., & Simon, T. 2005, *AJ*, 129, 829
- Danby, G., Flower, D. R., Valiron, P., Schilke, P., & Walmsley, C. M. 1988, *MNRAS*, 235, 229
- Deharveng, L., Lefloch, B., Zavagno, A., Caplan, J., Whitworth, A. P., Nadeau, D., & Mart  n, S. 2003, *A&A*, 408, L25
- Deharveng, L., Zavagno, A., & Caplan, J. 2005, *A&A*, 433, 565
- Dobashi, K., Bernard, J.-P., Yonekura, Y., & Fukui, Y. 1994, *ApJS*, 95, 419
- Dobashi, K., Yonekura, Y., Matsumoto, T., Momose, M., Sato, F., Bernard, J.-P., & Ogawa, H. 2001, *PASJ*, 53, 85
- Duerr, R., Imhoff, C. L., & Lada, C. J. 1982, *ApJ*, 261, 135
- Evans, N. J., et al. 2009, *ApJS*, 181, 321
- Fountain, W. F., Gary, G. A., & Odell, C. R. 1983, *ApJ*, 269, 164
- Furuya, R. S., Kitamura, Y., Wootten, A., Claussen, M. J., & Kawabe, R. 2003, *ApJS*, 144, 71
- Genzel, R., Ho, P. T. P., Bieging, J., & Downes, D. 1982, *ApJL*, 259, L103
- Herbig, G. H. 1958, *ApJ*, 128, 259
- Ho, P. T. P., & Townes, C. H. 1983, *ARA&A*, 21, 239
- Gandolfi, D., et al. 2008, *ApJ*, 687, 1303
- Kun, M., Balog, Z., Kenyon, S. J., Mamajek, E. E., & Gutermuth, R. A. 2009, *ApJS*, 185, 451
- Kutner, M. L., & Ulich, B. L. 1981, *ApJ*, 250, 341
- Lada, E. A. 1992, *ApJL*, 393, L25
- Lada, E. A., Evans, N. J., II, & Falgarone, E. 1997, *ApJ*, 488, 286
- Ladd, E. F., Myers, P. C., & Goodman, A. A. 1994, *ApJ*, 433, 117
- Laugalys, V., & Straizys, V. 2002, *Baltic Astronomy*, 11, 205
- Lang, K. R., & Willson, R. F. 1980, *ApJ*, 238, 867
- Leisawitz, D., Bash, F. N., & Thaddeus, P. 1989, *ApJS*, 70, 731
- MacLaren, I., Richardson, K. M., & Wolfendale, A. W. 1988, *ApJ*, 333, 821
- Matzner, C. D., & McKee, C. F. 2000, *ApJ*, 545, 364
- Myers, P. C., & Benson, P. J. 1983, *ApJ*, 266, 309
- Myers, P. C., Dame, T. M., Thaddeus, P., Cohen, R. S., Silverberg, R. F., Dwek, E., & Hauser, M. G. 1986, *ApJ*, 301, 398
- Nakajima, T., et al. 2007, *PASJ*, 59, 1005

- Prasad, S. S., & Huntress, W. T., Jr. 1980, ApJS, 43, 1
- Ridge, N. A., Wilson, T. L., Megeath, S. T., Allen, L. E., & Myers, P. C. 2003, AJ, 126, 286
- Rieke, G. H., & Lebofsky, M. J. 1985, ApJ, 288, 618
- Rohlfs, K., & Wilson, T. L. 1996, Tools of Radio Astronomy, XVI, 423 pp. 127 figs., 20 tabs.. Springer-Verlag Berlin Heidelberg New York. Also Astronomy and Astrophysics Library,
- Straizys, V., & Laugalys, V. 2008, Baltic Astronomy, 17, 143
- Sugitani, K., Fukui, Y., Mizuni, A., & Ohashi, N. 1989, ApJL, 342, L87
- Sugitani, K., Fukui, Y., & Ogura, K. 1991, ApJS, 77, 59
- Sugitani, K., & Ogura, K. 1994, ApJS, 92, 163
- Swift, J. J., & Welch, W. J. 2008, ApJS, 174, 202
- Tieftrunk, A. R., Megeath, S. T., Wilson, T. L., & Rayner, J. T. 1998, A&A, 336, 991
- Ungerechts, H., Walmsley, C. M., & Winnewisser, G. 1980, A&A, 88, 259
- Ungerechts, H., Winnewisser, G., & Walmsley, C. M. 1982, A&A, 111, 339
- Walborn, N. R. 2007, arXiv:astro-ph/0701573
- Walmsley, C. M., & Ungerechts, H. 1983, A&A, 122, 164
- Wendker, H. J. 1984, A&AS, 58, 291

Table 1. Line parameters obtained at the peak position of the clumps and the subclumps

Clump	R.A. (J2000)	Decl. (J2000)	Line (J, K)	T_{MB}^* (K)	v_{LSR}^\dagger (km s ⁻¹)	Δv^\ddagger (km s ⁻¹)	$\int T_{\text{MB}} dv^\S$ (K km s ⁻¹)	rms noise (K)
A1	20 ^h 58 ^m 18 ^s .8	+43°53′24″	(1,1)	1.92	5.6	1.5	2.96±0.13	0.10
			(2,2)	0.43	5.0	1.2	0.55±0.15	0.11
			(3,3)	≤0.30 [§]	0.10
A2	20 ^h 58 ^m 02 ^s .1	+43°53′24″	(1,1)	2.59	5.5	1.4	3.85±0.09	0.07
			(2,2)	0.56	5.4	1.6	0.93±0.11	0.08
			(3,3)	≤0.21 [§]	0.07
A3	20 ^h 57 ^m 45 ^s .5	+43°53′24″	(1,1)	1.44	5.3	2.1	3.21±0.13	0.08
			(2,2)	0.38	5.0	2.7	1.11±0.12	0.08
			(3,3)	≤0.24 [§]	0.08
B	20 ^h 56 ^m 49 ^s .9	+43°43′24″	(1,1)	2.79	1.5	1.9	6.25±0.21	0.14
			(2,2)	0.70	1.5	1.8	1.58±0.20	0.14
			(3,3)	≤0.42 [§]	0.14

* The error of the Gaussian fitting is close to the rms noise level.

† The error of the Gaussian fitting is much smaller than the velocity resolution (0.39 km s⁻¹).

‡ The error corresponds to one standard deviation.

§ The upper limit is given as 3 times of the rms noise.

Table 2. Physical properties of the clumps and the subclumps

Clump	Size (pc)	$\tau_{(1,1)}$	T_{rot} (K)	$N(\text{NH}_3)$ (cm ⁻²)	M_{LTE} (M_\odot)	M_{vir} (M_\odot)
A1	0.21	1.4±0.4	12±2	2.4×10 ¹⁵	12	...
A2	0.31	1.2±0.3	13±1	1.8×10 ¹⁵	20	...
A3	0.21	0.8±0.4	15±2	1.8×10 ¹⁵	9	...
A	0.67	1.2±0.2	13±1	1.8×10 ¹⁵	95	125
B	1.02	1.6±0.2	11±1	3.7×10 ¹⁵	452	350

Table 3. Star formation efficiency of individual clumps

Clump	Number of sources		Stellar mass (M_\odot)		SFE (%)	
	T-Tauri	Total	T-Tauri	Total	T-Tauri	Total
A1	5	< 15	6.9	< 19.9	36	< 62
A2	1	< 5	0.8	< 6.0	4	< 23
A3	0	< 4	0	< 5.2	0	< 36
A	7	< 32	7.7	< 41.5	8	< 30
B	0	< 24	0	< 31.2	0	< 6

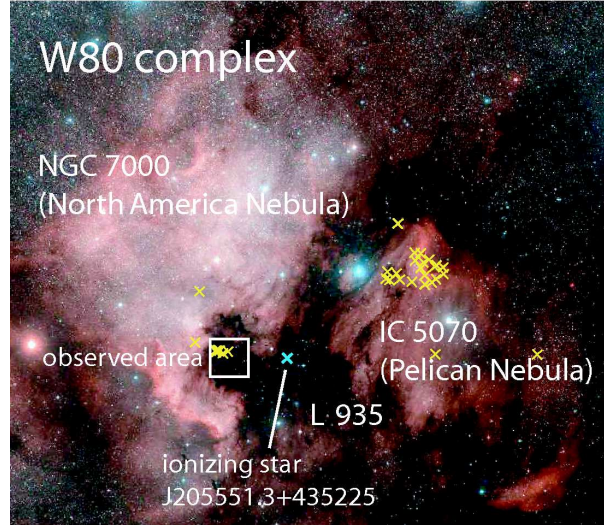


Fig. 1. Optical image of the W80 region (CalTech/Palomar) that comprises two H II regions of NGC 7000 (North America nebula) and IC 5070 (Pelican nebula) and dark lanes of L935. Yellow crosses show the positions of T-Tauri type stars (Herbig 1958). A blue cross shows the position of an O5 V type star (Comerón & Pasquali 2005).

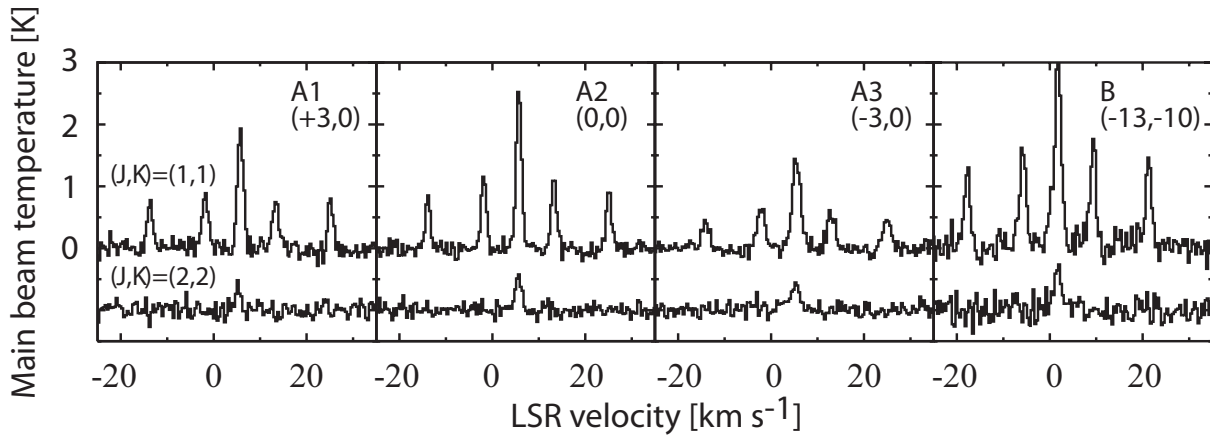


Fig. 2. Spectra in the NH_3 $(J,K)=(1,1)$ and $(2,2)$ lines observed at the peak position of the subclumps and the clump-B. The position offsets in arcmin from $(\alpha, \delta)_{(J2000)} = (20^{\text{h}}58^{\text{m}}02^{\text{s}}.1, +43^{\circ}53'24'')$ are shown in the top-right corner.

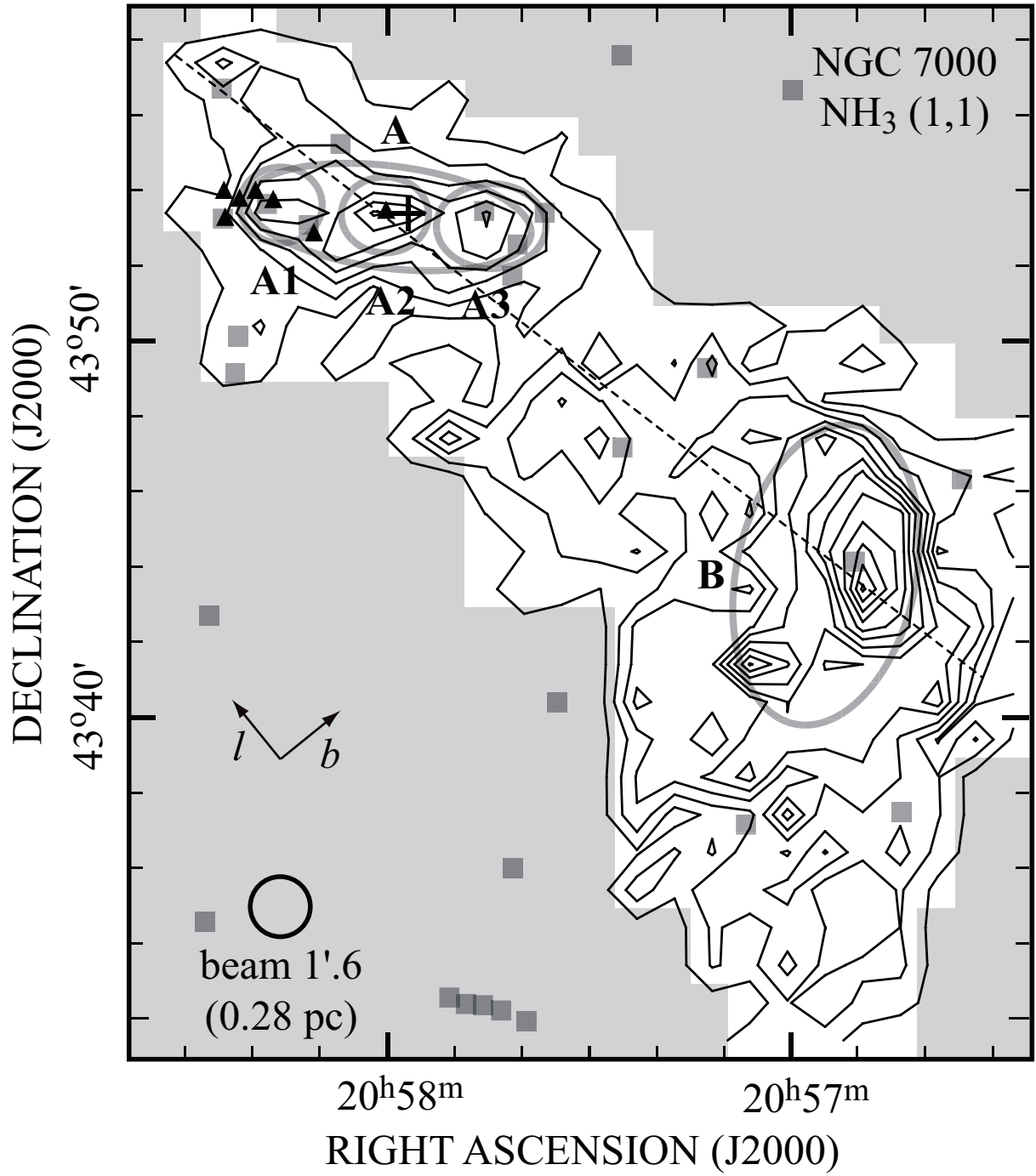


Fig. 3. Integrated intensity map of the main hyperfine component of the NH₃ (1,1) line. The lowest contour and the contour interval are 0.3 and 0.6 K km s⁻¹, respectively. The circle in the bottom-left corner shows the beam size. The gray ellipses show the extents of the clumps and the subclumps. The triangles and squares show the T-Tauri stars and MSX sources, respectively. The cross shows the position of the H₂O maser. The dashed line shows the axis of the position velocity map shown in Figure 6.

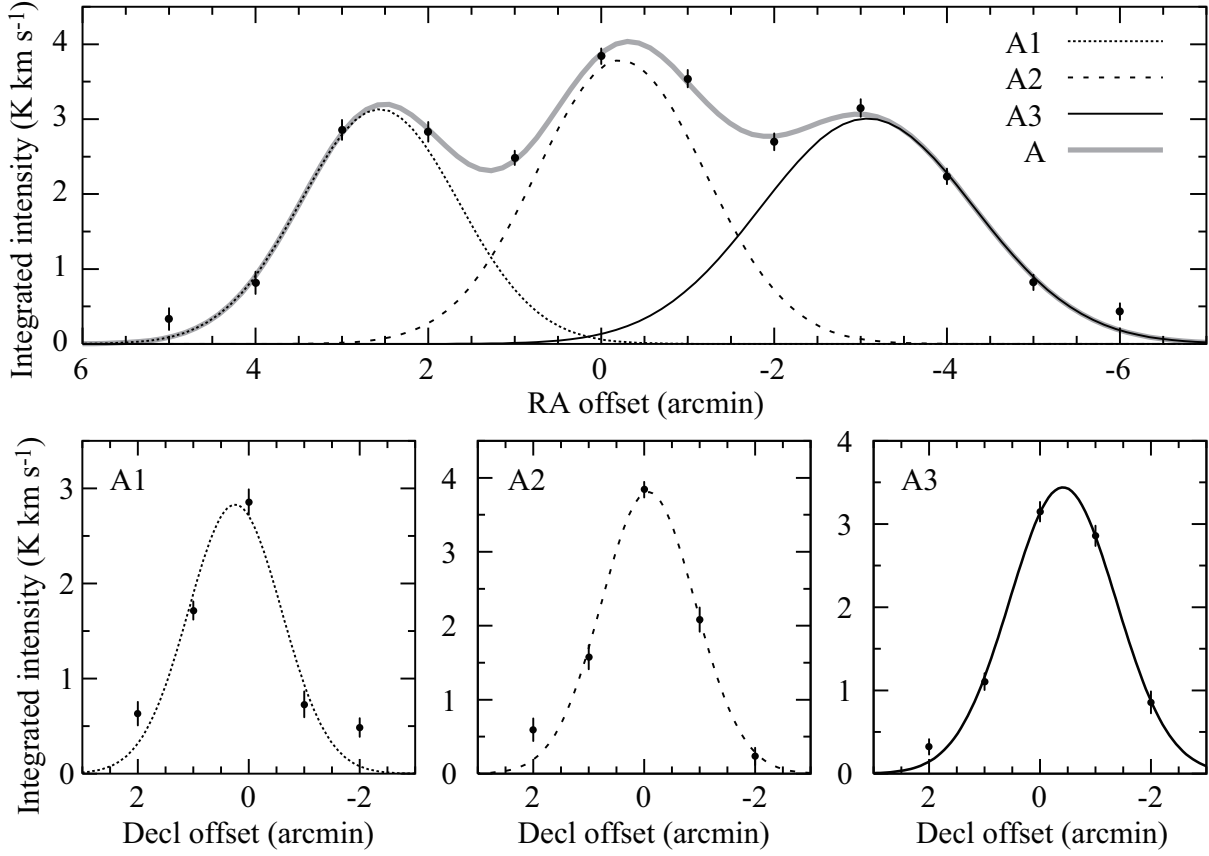


Fig. 4. The results of the Gaussian fitting to the intensities along the right ascension and declination for subclump A1–A3. The position offsets in arcmin from $(\alpha, \delta)_{(J2000)} = (20^{\text{h}}58^{\text{m}}02^{\text{s}}.1, +43^{\circ}53'24'')$ are shown.

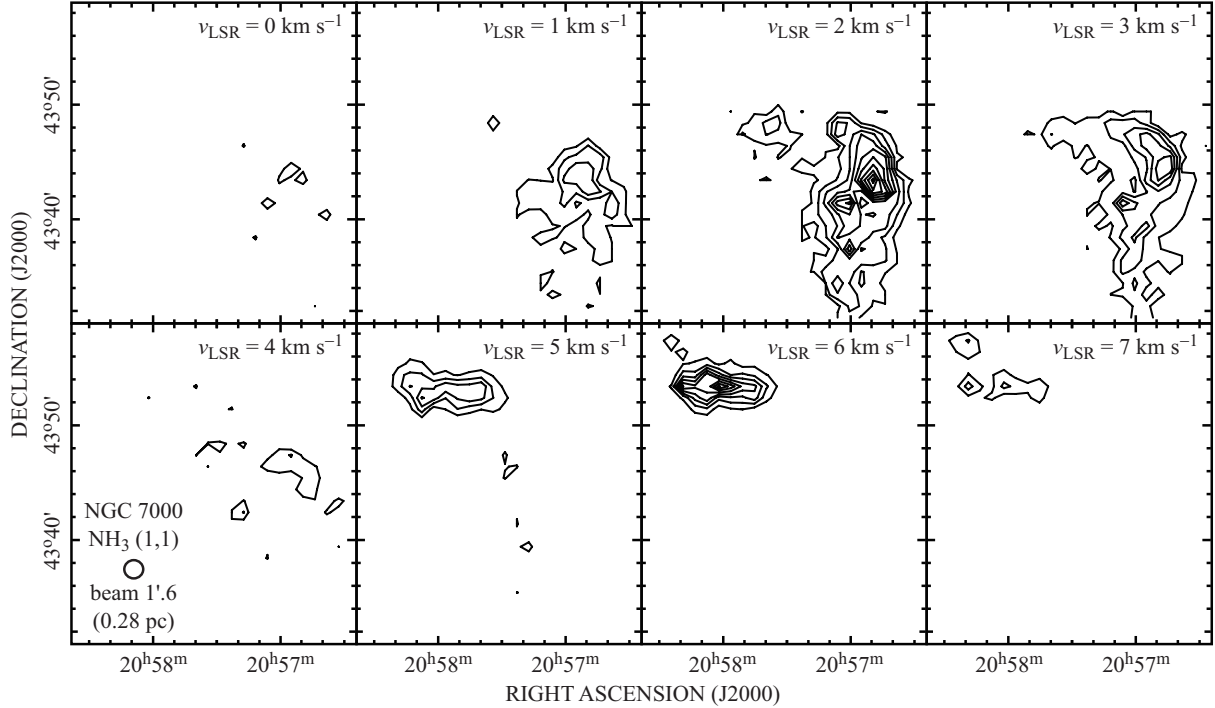


Fig. 5. Velocity channel maps in the NH₃ (J, K)=(1,1) line. The lowest contour and the contour interval are 0.3 and 0.3 K, respectively. The intensity is averaged in the velocity span of 1 km s⁻¹.

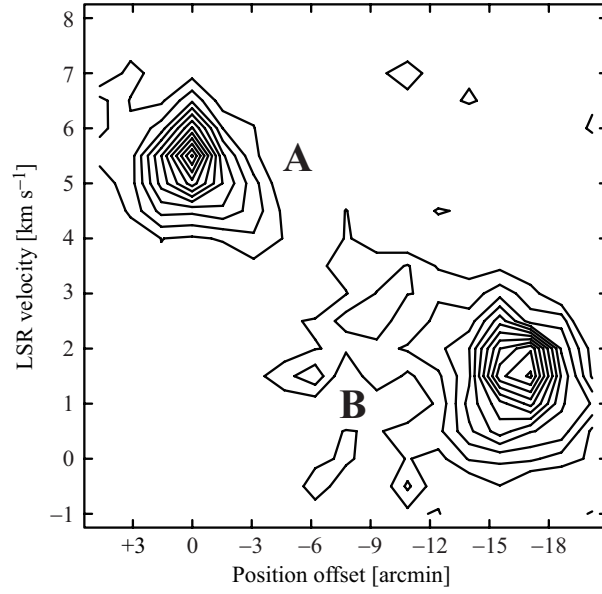


Fig. 6. Position-velocity map of the whole cloud in the NH₃ (J,K)=(1,1) line. The lowest contour and the contour interval are 0.2 and 0.2 K at the T_{MB} unit, respectively. The position offset is relative to the position at $(\alpha, \delta)_{(\text{J2000})} = (20^{\text{h}}58^{\text{m}}02^{\text{s}}.1, +43^{\circ}53'24'')$ along the dashed line shown in Figure 3.

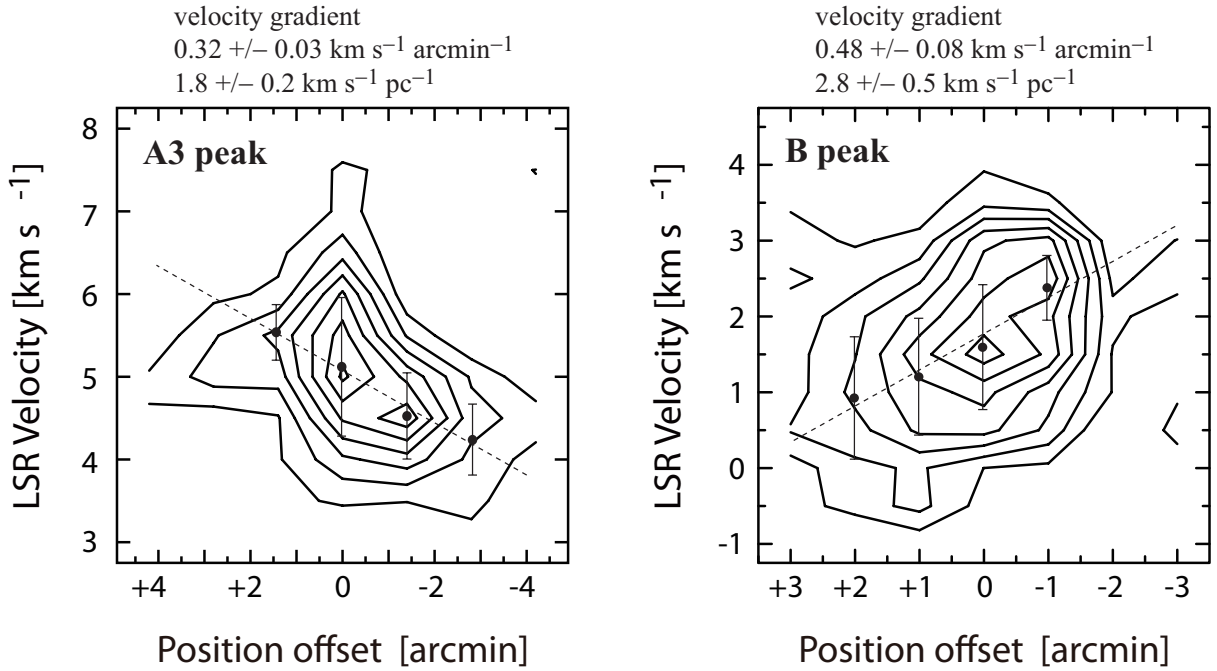


Fig. 7. Position-velocity maps of the NH₃ (J,K)=(1,1) line toward subclump-A3 (left) and clump-B (right). The lowest contour and the contour interval are 0.3 and 0.3 K, respectively. The position offset is relative to the peak positions at $(\alpha, \delta)_{(\text{J2000})} = (20^{\text{h}}57^{\text{m}}45^{\text{s}}.5, +43^{\circ}53'24'')$ along the position angle of 45° for the A3 peak and $(20^{\text{h}}56^{\text{m}}49^{\text{s}}.9, +43^{\circ}43'24'')$ along the position angle of 90° for the B peak.

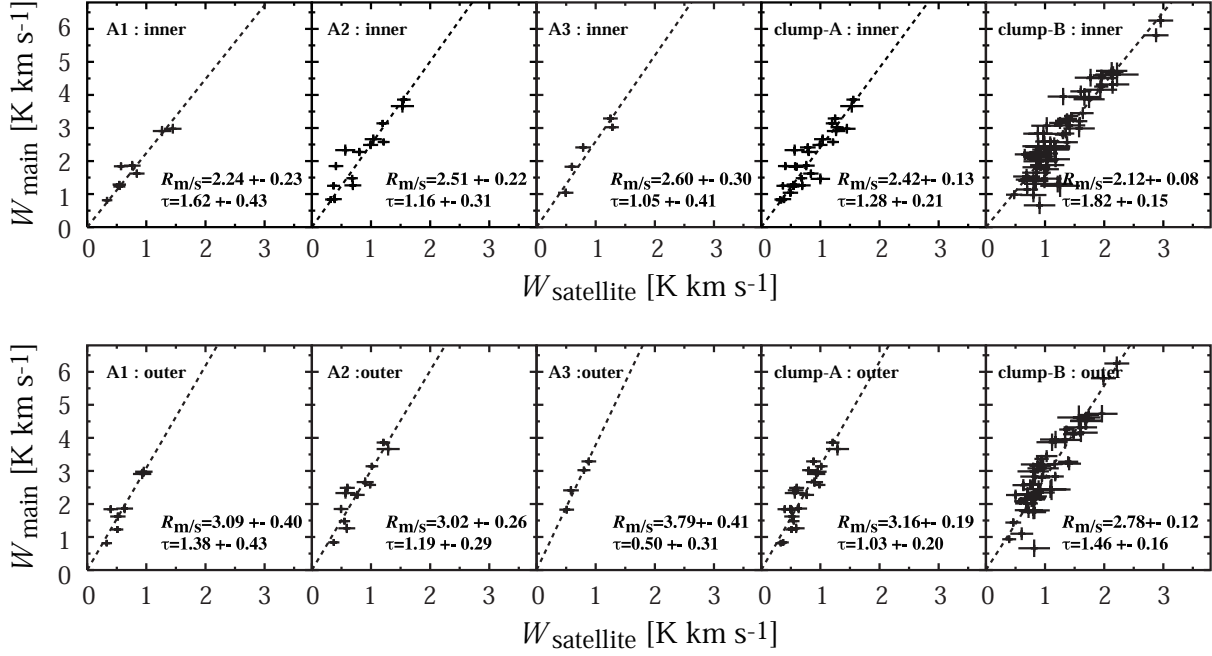


Fig. 8. Correlations of the integrated intensity in the (1,1) main and satellite lines. The correlations of the main to the inner and outer satellite lines are shown in the top and bottom panel, respectively. The data detected over the 3σ level in both the main and the satellite lines are plotted. The error bar shows the rms noise (1σ). The estimated optical depth is shown in the bottom of each panel.

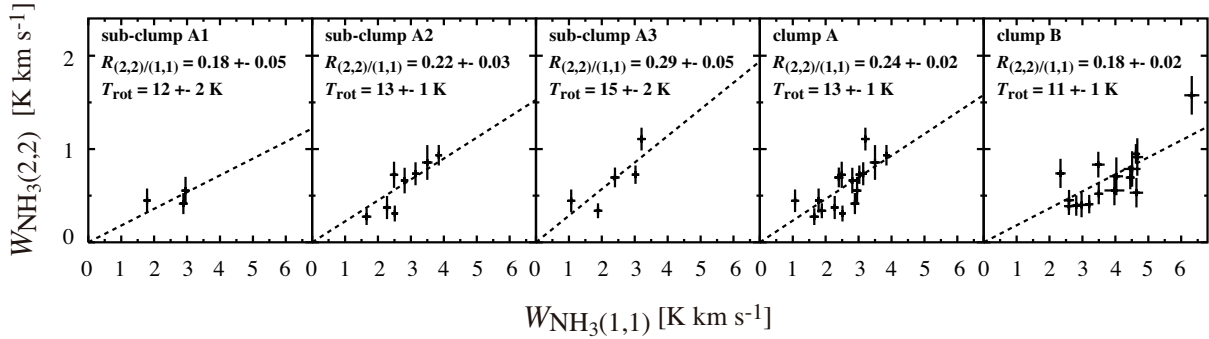


Fig. 9. Correlations of the integrated intensity in the (1,1) and (2,2) lines. The data detected over the 3σ level in both the (1,1) and the (2,2) lines are plotted. The error bar shows the rms noise (1σ). The estimated T_{rot} is shown in each panel.

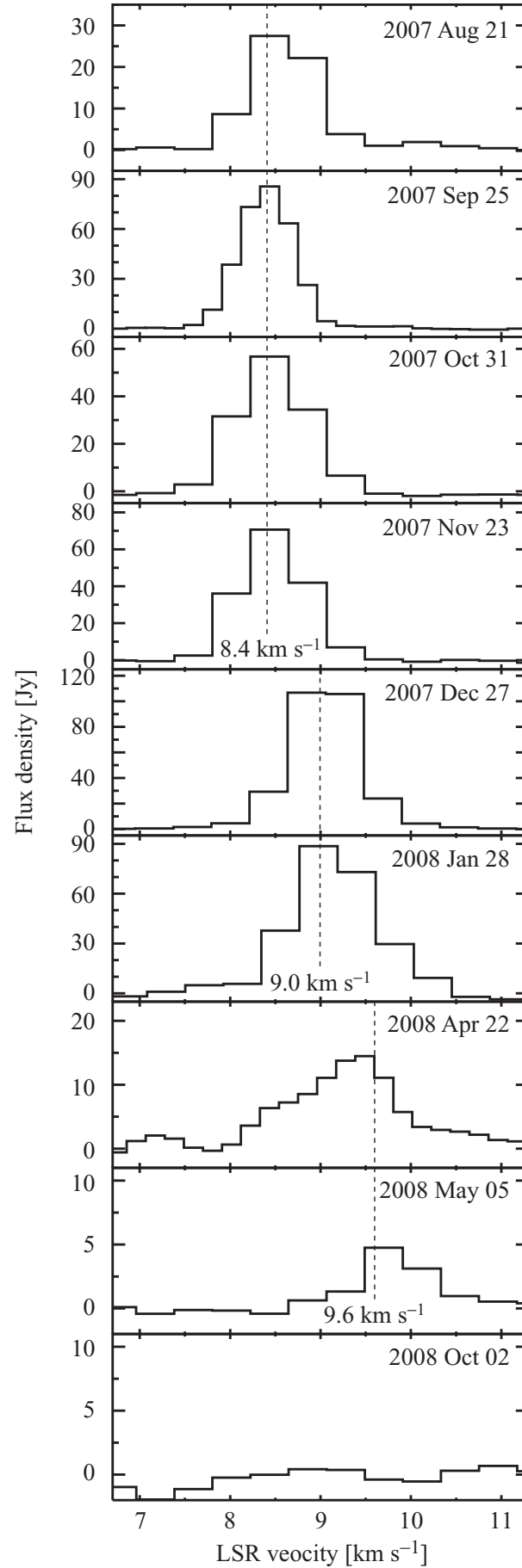


Fig. 10. H₂O maser spectra obtained by our single-dish monitoring observations. Two velocity jumps are found between November and December of 2007, and between January and April of 2008. The maser emission disappeared in October 2008.

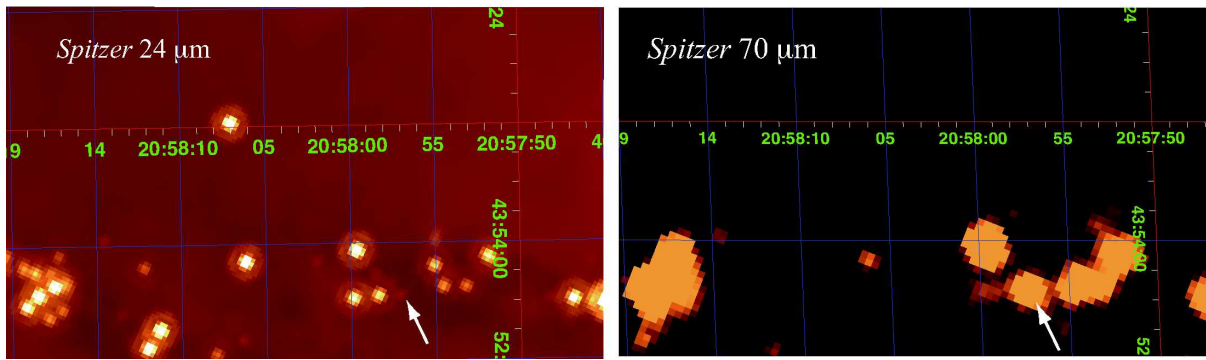


Fig. 11. *Spitzer* images at 24 μm (left) and 70 μm (right). A white arrow shows the position of the H₂O maser.

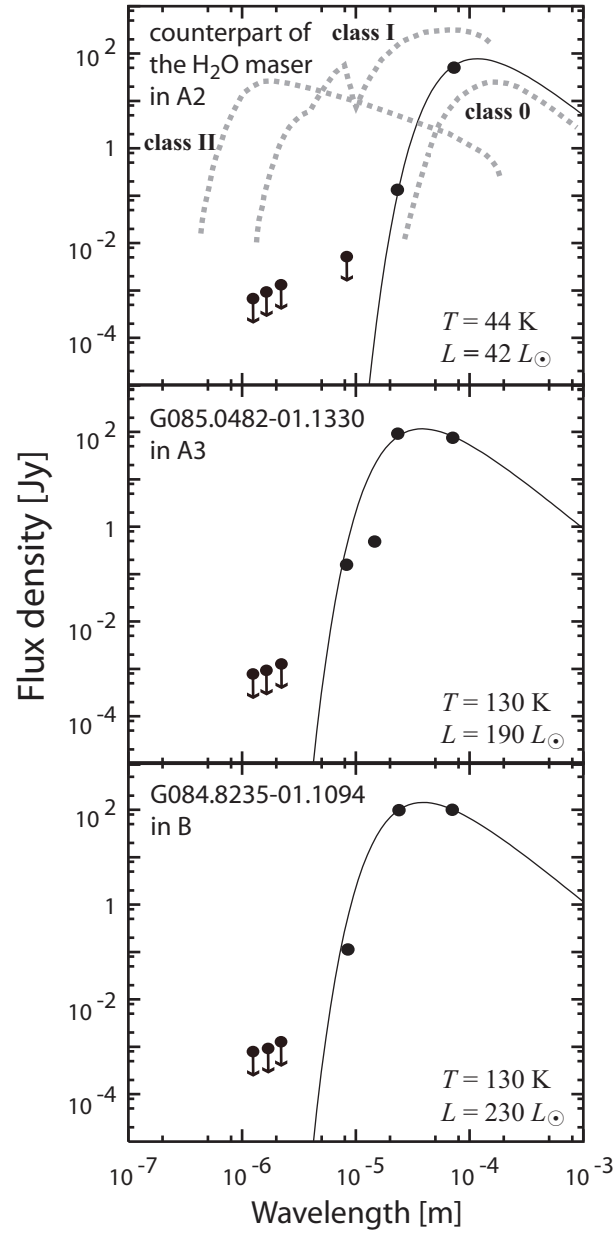


Fig. 12. Spectral energy distribution of the three infrared sources. The solid line shows the best fit blackbody with parameters shown at the right-bottom corner in each panel. The gray dashed lines in the top panel show typical spectra of class 0, I, and II (Bachiller 1996).

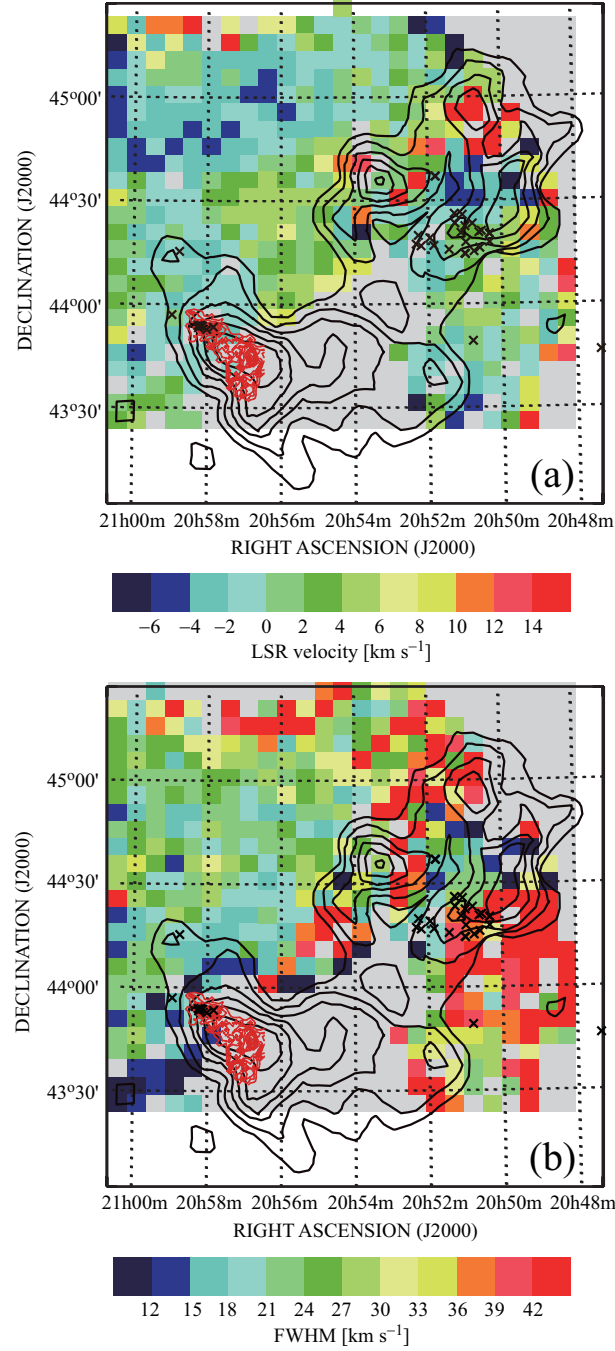


Fig. 13. (a) The LSR velocity map of the H α emission (color; Fountain et al. 1983) on which the ^{13}CO integrated intensity map (black contour; Dobashi et al. 1994) and the NH_3 (1,1) integrated intensity map (red contour) are superimposed. The black cross is the emission line star (Herbig 1958). (b) The FWHM map of the H α emission (color; Fountain et al. 1983) superimposed on the same maps as that shown in (a).

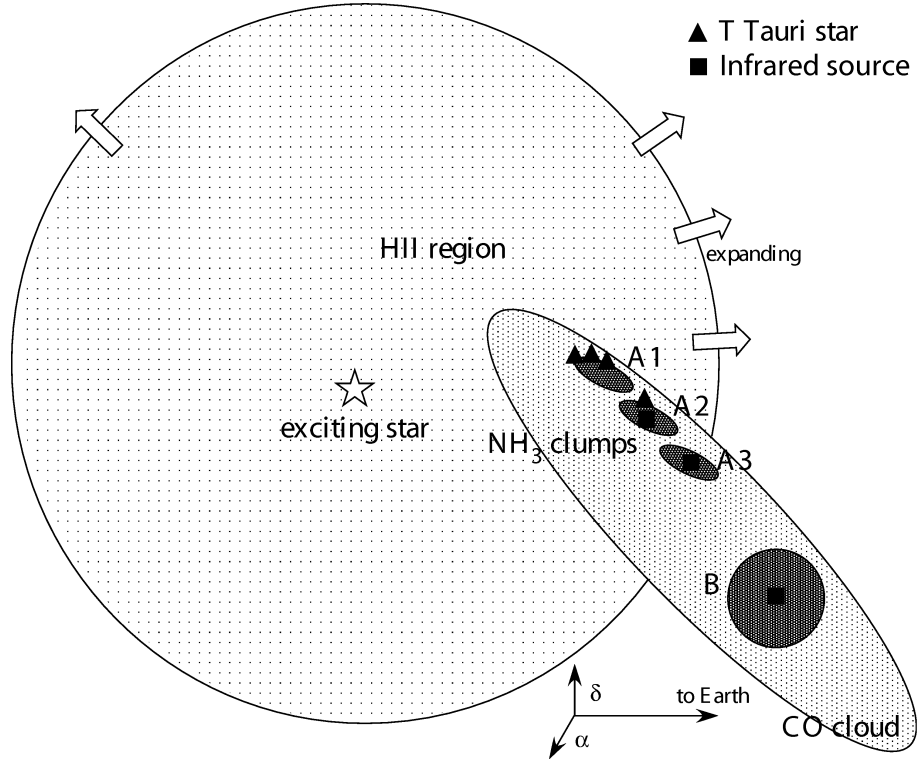


Fig. 14. Schematic geometry of the NH₃ clumps and the H II region.

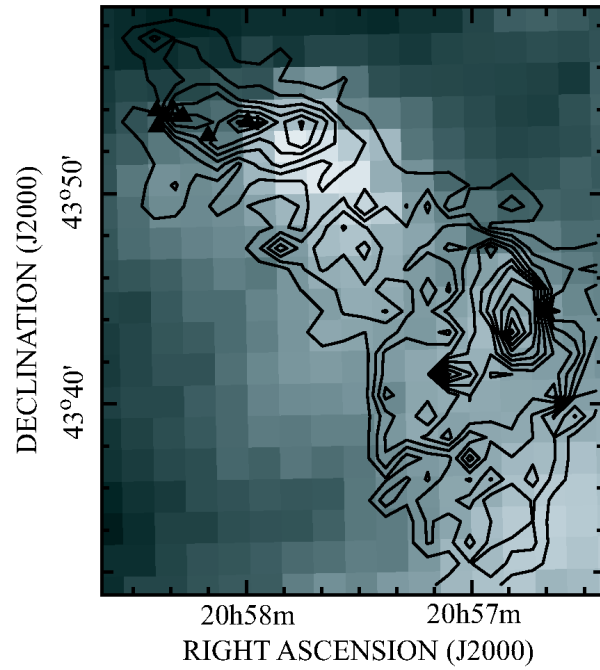


Fig. 15. IRAS 100 μ m image (gray scale) on which the integrated intensity map of NH₃ (1,1) line (contour) is superimposed.